JrnlID 10494_ArtID 9163_Proof# 1 - 09/06/08

Flow Turbulence Combust
DOI 10.1007/s10494-008-9163-1

Turbulent Flow and Dispersion of Inertial Particles in a Confined Jet Issued by a Long Cylindrical Pipe

Fabio Sbrizzai · Roberto Verzicco · Alfredo Soldati

Received: 22 November 2007 / Accepted: 29 May 2008

Abstract In this work we examine first the flow field of a confined jet produced by a turbulent flow in a long cylindrical pipe issuing in an abrupt angle diffuser. Second, we examine the dispersion of heavy micro-particles entrained by the turbulent flow. Specifically, we examine how the particle dispersion field evolves in the multiscale flow generated by the interactions between the large-scale structures, which are geometry dependent, with the smaller turbulent scales issued by the pipe which are advected downstream. We use Large-Eddy-Simulation (LES) for the flow field and Lagrangian tracking for particle dispersion. The complex shape of the domain is modelled using the immersed-boundaries method. Fully developed turbulence inlet conditions are derived from an independent LES of a spatially periodic cylindrical pipe flow. The flow field is analyzed in terms of local velocity signals to determine spatial coherence and decay rate of the coherent K–H vortices and to make quantitative comparisons with experimental data on free jets. Particle dispersion is analyzed in terms of statistical quantities and also with reference to the dynamics of the coherent structures. Results show that the particle dynamics is initially dominated by the Kelvin–Helmholtz (K–H) rolls which form at the expansion and only eventually by the advected smaller turbulence scales.

Keywords Turbulent flow · Dispersion · Inertial particles

F. Sbrizzai · R. Verzicco · A. Soldati
Centro Interdipartimentale di Fluidodinamica e Idraulica, and Dipartimento di Energetica e Macchine, Università di Udine 33100, Udine, Italy

R. Verzicco
Dipartimento di Ingegneria Meccanica e Gestionale and Centre of Excellence for Computational Mechanics (CEMeC), Politecnico di Bari, 70125 Bari, Italy

A. Soldati (✉)
International Center for Mechanical Sciences, CISM, Udine, Italy
e-mail: soldati@uniud.it

1 Introduction

The dispersion of inertial particles in a cylindrical diffuser is an issue present in a number of technological applications. In most of the applications, the crucial parameter is often the degree of interphase mixing achieved downstream the diffuser. The behavior of the particle-flow system is complex and characterized by a number of different spatial and temporal scales mutually interacting and contributing to the particle dispersion. Examples of a recent application to dispersed reacting flow are referenced in [1].

Particle distribution in pipes and channels is dominated by local interactions with wall turbulence which induce local segregation [2–4] and in turn stable distribution patterns with a large concentration of particles flowing near the walls following the elongated streaks [5]. If a wide angle diffuser is present along the pipe, a strong change in the nature of the turbulence field is expected, with corresponding strong modifications for particle distribution and dispersion. Large-scale coherent structures produced by the Kelvin-Helmholtz instability (rings) interact in a three-dimensional fashion with the turbulence structures issuing from the pipe; particle distribution is therefore determined by the interactions between large-scale structures and the smaller-scale structures typical of the pipe flow, which are advected downstream.

The configuration of the pipe and diffuser can be considered a combination of known fluid dynamics canonic cases such as a long pipe, a round jet and a backward-facing step. A combination of the vortical structures observed in these cases can be expected to control the dispersion of particles. These structures include (i) the small turbulence scales issuing from the long pipe and (ii) the large scale structures generated by the presence of the abrupt diffuser and produced by primary instabilities of the shear layer. It is not clear how these different scale structures interact in this specific flow configuration and whether their interaction can eventually trigger the formation of a three-dimensional, incoherent vorticity field downstream the diffuser which may play a significant role in particle dispersion. The practical motivation for this work is thus the necessity to understand and model the physics of particle dispersion in multiphase confined jets. Even though this configuration is rather common to many industrial applications, there are few detailed simulations of the turbulent jet issuing from a cylidrical pipe in a larger pipe. In practice, industrial cases are computed with coarse-grained methods (RANS and averaged diffusion-type Eulerian descriptions) used with scarce possibility of benchmark or error evaluation and without a thorough understanding of the effect produced by some specific modelling assumptions (for instance, the inlet boundary conditions and the extent of the computational domain) on the results produced by the numerical simulation.

In a previous work [6] we examined the flow field in a large angle diffuser, and we considered the response of different size particles to the three dimensional structures generated by a jet evolving in a confined domain. However, that preliminary work had two main computational limits: the first was the length of the computational domain which was insufficient to develop complex three-dimensional instabilities. The second limitation was the inlet boundary condition: the inlet flow was analytically prescribed without taking into account the near–wall turbulence structures of the preceding turbulent pipe.

In this work, our object is first to characterize the influence of inlet turbulence on particle dispersion. Second, we want to give physical insights to model the influence

of non-isotropic structures dominating particle dispersion. Finally, we wish to build a benchmark for the simulation of multiphase confined jets to be used for the validation of current commercial code applications and models.

In Fig. 1 it is possible to compare the numerical approach adopted for the previous and for the current work. The dashed line indicates the extent of the domain used in our previous work. One of the main results of that work was the description of the radial dispersion mechanism for small particles. This mechanism depends on the secondary structures formed by the instability occurring in the Kelvin-Helmholtz rolls. In that work, however, due to the limited extent of the computational domain downstream the diffuser accommodating only for three Kelvin-Helmholtz rolls, it was not possible to examine in detail the interactions of two consecutive Kelvin-Helmoltz rolls and their effect on particle transport and dispersion. These phenomena can be now observed, being the streamwise length of the domain after the expansion more than twice longer than in the previous investigation. A second

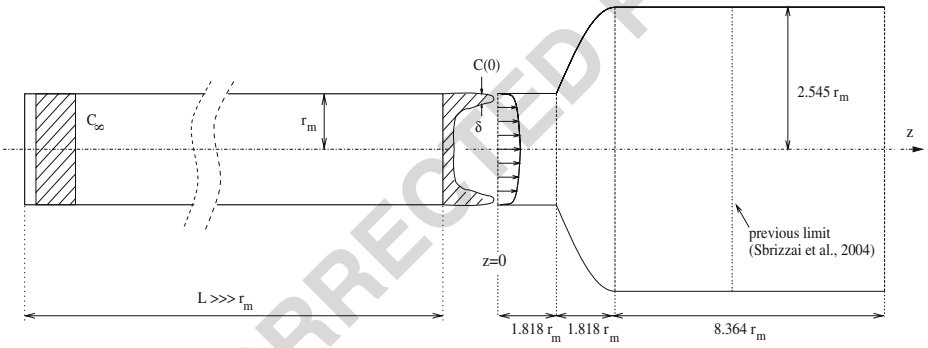

(a)

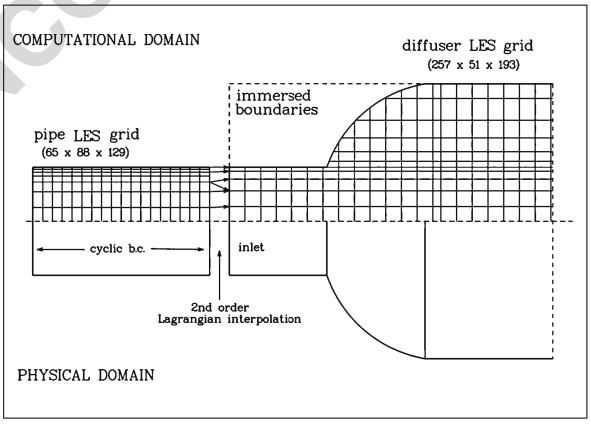

(b)

Fig. 1 **a** Dimensions and shape of the computational domain used for the Large-Eddy Simulation of the diffuser; inlet velocity profile and the initial particle radial concentration distribution $C(0)$ are schematically shown. **b** Schematics of the pipe-diffuser grid coupling; a different grid is used for DNS and for LES calculations, thus requiring a second−order Lagrangian interpolation

major main investigation is pursued in this study, which concerns the influence of the initial turbulence conditions on the evolution of the flow structures and on particle dispersion. Our aim is to simulate a jet issued from a long pipe in which turbulence has had enough time to fully develop. A complete solution of the entire flow (long pipe and diffuser) would be hardly feasible from a computational viewpoint owing to the large spatial dimensions of the system. To circumvent this problem, several techniques for mimicking inlet turbulence have been proposed in the literature, ranging from exploiting random perturbation [7], to the case of an independent direct numerical simulation (DNS) of the upward stretch of the pipe. To the best of our knowledge, the last technique has been successfully used by Akselvoll and Moin [8] in confined, coannular round jets and by Na and Moin [9] in a backward facing step exploiting inlet profiles calculated by an independent pipe/channel periodic flow simulation. We decided to follow Na and Moin [9] and we took "slices" from an independent large-eddy-simulation (LES) of a turbulent pipe flow to represent the inlet conditions for the diffuser. Compared to our previous work, we can thus (i) investigate flow structures in the surroundings of the jet core issued from a fully-turbulent pipe; (ii) investigate the flow evolution many diameters downstream of the expansion where the interaction between the large-scale structures occurs; (iii) study the behavior of inertial particles of several diameters dispersed in such flow field.

The jet flow can be roughly divided into two regions, a *transitional* and a *turbulent* region whose features can be summarized as follows: the transitional region [10] is characterized by a specific sequence of large structures that, although becoming progressively irregular, maintain their initial "identity" (i.e. they do not interact with other structures). This region corresponds to that investigated by Sbrizzai et al. [6]. Farther downstream, the interaction between the transitional structures produces a fully three-dimensional vorticity field [10], indicating the presence of differently oriented vortices spanning a wide range of spatial and temporal scales.

As described in Sbrizzai et al. [6], both coherent and non-coherent structures are generated by different kinds of instability originating within the shear layer of the jet. In particular a Kelvin–Helmholtz instability occurs about one inlet-pipe diameter downstream of the separation point producing the vortex rings. The primary Kelvin–Helmholtz instability [10–13] is followed by a secondary instability which is responsible for outward directed radial fluid bursts observed in between contiguous vortex rings. Simultaneously, spatially-periodic, quasi streamwise vortex pairs (rib–vortices) are formed on both sides of each burst. Owing to the intense strain rate, rib–vortices are stretched along the *diverging separatrix* of the rings [13] thus reducing the diameter of the former and increasing their lifetime.

In the downstream part of the transitional region, due to different advection velocity, vortex rings undergo a pairing process during which they engulf rib–vortices and produce smaller scale three–dimensional vortices eventually degenerating to turbulence.

To reproduce accurately the described flow features, it is necessary to resolve explicitly both the large-scale coherent structures and the smaller vortices within the eddies and to resource to modelling only for the finer and more homogeneous structures. To this purpose, we used the Large-Eddy simulation code developed by Verzicco and Orlandi [14], which we already used in our previous work [6].

The behavior of inertial micro-particles is then investigated using a Lagrangian tracking algorithm. In this work, particles are very small but heavy. Their diameter

is smaller than any relevant flow scale and they respond to the flow field via their inertia, which is usually scaled by the characteristic time required to attain a steady state after a perturbation. We remark that the response to the flow structures varies according to the particle−to −structure timescale ratio (Stokes number, St).

At present, there is no simulation available from the literature of dispersed flow after an abrupt expansion which can be used as a reference benchmark to test simple model and CFD results. We believe that the present simulation may represent a significant step in this direction. We underline here that also experiments to assess dispersed flow simulations are not only rare but also include one specific problem associated with the knowledge of inlet conditions, which are usually hard to specify experimentally, thus inducing an extra source of uncertainty for benchmarking numerical simulations [15]. With this paper, we are trying to fulfill the demand for quantitative and reproducible accurate data in the simplest framework for multiphase flow modelling and yet capturing all the essential qualitative physics. Furthermore, observations on the evolution of the unsteady structures of the flow allowed us to understand how interactions among the large-scale vortices produced by primary instabilities of the shear layer eventually lead to the formation of a three-dimensional, incoherent vorticity field which plays a significant role in particle dispersion.

The work is organized as follows: initially the computational methodology is described for the flow field and particle dispersion. The results are then presented and discussed by instantaneous flow visualization and statistical indicators. Conclusions are finally given along with possible future developments.

2 Methodology

For the purposes of the present work, which was initially inspired to an exhaust gas pipe for automotive engines, the simulated fluid is air at 600 K with density $\rho = 0.965\ kg/m^3$ and kinematic viscosity $\nu = 1.57 \cdot 10^{-5}\ m^2/s$. The typical bulk velocity is $U_b = 5.0\, m/s$, corresponding to a Reynolds number of:

$$Re = \frac{2r_m \cdot U_b}{\nu} = 17516, \tag{1}$$

where $r_m = 0.0275\ m$ is the radius of the inlet section. In this paper, all length and velocity scales are made dimensionless by r_m and U_b, respectively. The reference time scale can also be computed from r_m and U_b as:

$$\tau = \frac{r_m}{U_b} = 5.5 \cdot 10^{-3}\ s. \tag{2}$$

The simulated physical domain is sketched in Fig. 1a, where a large opening angle diffuser placed at the end of a long pipe is shown. Specifically, two separate computational domains are used to perform two different simulations: (i) an upstream, periodic pipe, necessary to provide a fully-developed turbulent flow, and (ii) the diffuser, coupled to a suitably long portion of the downstream pipe. In both cases, the geometry is axisymmetric with respect to the axial coordinate, z. The frame of reference is cylindrical with r and θ the radial and azimuthal coordinates, respectively.

The flow in both the inlet pipe (left in Fig. 1a) and in the diffuser (right in Fig. 1a) are reproduced by Large-Eddy Simulation (LES). As shown in Fig. 1, the diffuser is preceded by a short portion of the inlet pipe; this is required to allow the adjustment of possible perturbations introduced by the interpolation of the periodic turbulent pipe simulation at the inflow section of the diffuser. This inlet pipe is also used to account for the two–way coupling between the pipe and diffuser flows which is produced by the elliptic nature of the Navier–Stokes equations. As shown by Ovchinnikov et al. [16] however, this last factor has only a marginal effect on the downstream flow and the present procedure gives satisfactory results.

The dimensions of the domain are shown in Fig. 1a; the length of the diffuser is 1.818 r_m, the radius of the downstream pipe is $R = 2.545\ r_m$ and its length is $L = 8.364\ r_m$ (that is more than twice the length we used previously [6] which was 3.636 r_m). We conventionally chose the origin of the streamwise axis z at the center of the inflow section of the diffuser computational domain.

2.1 Large Eddy simulation of the pipe

To obtain a fully-developed turbulent flow to be *fed* at the diffuser inlet, we performed a Large Eddy Simulation (LES) of a periodic pipe at $Re = 17\,516$. For this simulation, the code by Orlandi and Fatica [17] was used. This code has been used and validated in a previous work [3]. The only relevant change with respect to the original code is the implementation of a sub-grid-scale dynamic Smagorinsky model for the LES; the software is essentially the same as that used for the subsequent diffuser where further details on the LES procedure are given. The calculation of a fully-developed pipe flow would require a very long computational domain (of the order of hundreds of pipe diameters); this condition is computationally unfeasible and as a surrogate streamwise periodic boundary conditions are applied on a pipe section longer than the flow correlation length. Specifically, a 10 diameters long pipe was used, and calculations were carried out on a cylindrical grid (shown in Fig. 1a) with $65 \times 88 \times 129$ nodes in the azimuthal, radial and axial directions, respectively, for a time long enough to ensure converged statistics of the first and second order moments of the flow. Other boundary conditions are no-slip and no-cross boundary conditions applied at pipe walls for the velocity. Grid stretching is applied in the wall layer to capture the wall turbulence structures.

Figure 2 shows statistical quantities obtained from the pipe LES, made dimensionless by the friction velocity calculated as: $u_w = \sqrt{\tau_w/\rho}$, in which τ_w is the average shear stress at the wall and ρ is the fluid density. Specifically, Fig. 2a shows the average axial velocity profile, whereas Fig. 2b, c and d show the Root Mean Square (RMS) of the axial, radial and azimuthal velocity fluctuations, respectively. The time-average profile of Fig. 2a is compared with the Prandtl theoretical turbulent profile (the two dashed lines represent the viscous sublayer and the inertial sublayer, respectively). In all figures, the radial distance from the wall $(r_m - r)$ is made dimensionless by the wall length unit: $l_w = \nu/u_w$. The results of Fig. 2 have been obtained at $Re_\tau = 470$ and data at the same Reynolds number are not available for a comparison. Nevertheless in [18] similar cases are computed and the results compare well for the rms statistics of the three velocity components either for the peak values and for their spatial positions.

JrnlID 10494_ArtID 9163_Proof# 1 - 09/06/08

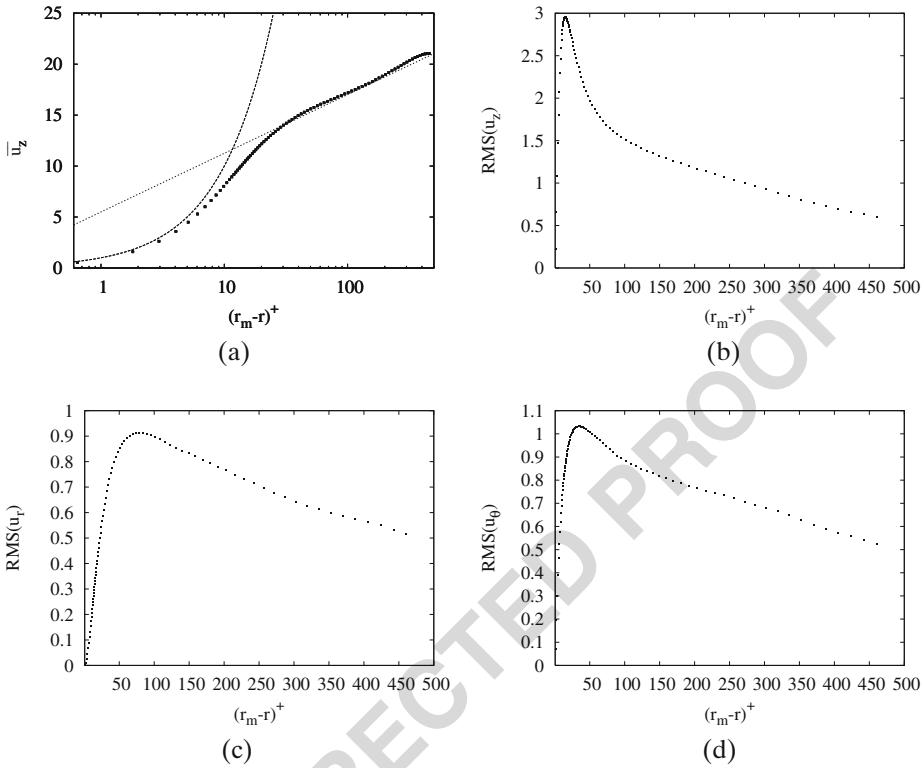

Fig. 2 Velocity statistics of the inlet conditions. Average axial velocity is shown in **a**, axial, radial and azimuthal velocity RMS are respectively shown in **b**, **c** and **d**. Scales are made dimensionless in wall units

The instantaneous velocity field calculated for the pipe over a long time period was stored to be used as input for the confined jet diffuser geometry.

2.2 Large-Eddy simulation of the confined jet

To solve for the three-dimensional Navier-Stokes equations in the computational domain sketched in Fig. 1a, the Large-Eddy Simulation (LES) code developed by Verzicco et al. [19] and by Orlandi and Fatica [17] (see also [20] for a thorough explanation of the method) and previously used [6] is employed. The LES code, provides a second–order accurate finite–difference discretisation in cylindrical coordinates for the spatial derivatives. The coordinates are indicated by θ, r and z in the azimuthal, radial and axial directions, respectively, and the computational grid has 257 (N_θ) $\times$ 51 (N_r) $\times$ 193 (N_z) nodes, as reported in Fig. 1b. The purpose of this figure is descriptive and only a small sample of the mesh is shown to compare the resolution of the long pipe and the diffuser. We report here some details regarding the grid. The grid spacing is uniform in the θ direction, with $\Delta\theta = 2\pi/(N_\theta - 1)$. In the jet shear layer this corresponds to approximately a spacing of $0.089r_m$. In the jet shear layer the grid spacing is minimum along r and corresponds to $\Delta r_{min} = 0.0266r_m$. In

the axial coordinate, z, the grid spacing is uniform along and equal to $L_z/(N_z - 1)$, corresponding to $\Delta z = 0.02625 r_m$.

Time-advancement is based on a 3^{rd} order low–storage Runge–Kutta (RK) scheme for the nonlinear terms in combination with a Crank–Nicholson for the viscous terms. The pressure-velocity coupling is handled by a fractional-step method [21, 22] that ensures incompressibility at each sub-step of the RK scheme. To model the sub-grid scales (SGS), not explicitly resolved by the grid, the SGS dynamic model developed by Germano et al. [23] was used. The dynamically computed constant of the Smagorinsky model is averaged in the azimuthal direction since it is a homogeneous direction for this flow. Negative values of the turbulent viscosity are allowed up to the limit of zero total viscosity (molecular plus turbulent, $\nu_T + \nu$); more negative values of ν_T are therefore clipped to $-\nu$. The radial grid is stretched to cluster the nodes in the shear layer where higher velocity gradients are expected and most of the smaller structures are formed. To achieve acceptable azimuthal resolution at the outer radial surface, the number of nodes in θ is relatively high (257 points) and in cylindrical coordinates the azimuthal resolution around the centerline becomes over-refined, as noted by Akselvoll and Moin [8]. This is not an issue in the present numerical procedure since the nonlinear terms in the azimuthal direction are treated implicitly and the azimuthal over-resolution does not influence the stability of the scheme; details on the changes needed by the scheme to implement the implicit time integration of the azimuthal derivative convective terms are given in [8] from which the present method has been derived.

Since the code solves the Navier–Stokes equations in a cylindrical domain – i.e. with the same radial extent over all z values – to model the walls of the diffuser and of the upstream pipe, the immersed-boundaries approach [24] is employed to set the velocity field to zero in all grid points which lie outside the walls, as shown in Fig. 1b.

Inlet boundary conditions for the diffuser are provided by the complementary turbulent pipe simulation. The coupling of the two simulations must handle the different grid size and time steps of the computations; this coupling was obtained by a second-order Lagrangian spatial interpolation of the velocity components and by a storage in time of r–θ planes of the pipe flow that were successively interpolated at the time required by the jet LES.

At the outlet, the convective conditions are used:

$$\frac{\partial u_z}{\partial t} + U_c \frac{\partial u_z}{\partial z} = 0, \tag{3}$$

thus ensuring that unsteady structures are advected by the mean flow outside the computational domain without reflections [9, 25, 26].

2.3 Lagrangian tracking

To track the particle dynamics we used a Lagrangian approach in which we follow the trajectory of each particle by integrating in time the Basset-Boussinesq-Oseen equation of motion [27].

As mentioned, the problem under study is a complex amalgama of several prototypical flows (shear layer, reattachment flow in a sudden expansion, turbulent channel flow) all of which are well-known and studied independently. To the best of our knowledge, this research is the first attempt to elucidate the physics of the influence of such complex turbulent field on particle dispersion and to provide a

quantitative database onto which simplified models (and RANS) could be calibrated. Therefore, we decided to run the simulation of particle dispersion under controlled conditions, minimizing the possible effect of modelling on results. The assumptions for particle modelling are: *(i)* all particles are non-interacting, non-deformable solid spheres; *(ii)* particle density is large compared to fluid density; *(iii)* the effect of the particles on the flow is neglected (the particle–to–fluid mass loading ratio being of the order of 10^{-5}); *(iv)* virtual mass, pressure gradient and Basset forces are neglected.

According to many previous works [1, 28, 29], the study of the order of magnitude of the forces acting on particles based on the equation of motion derived by Maxey and Riley [30] reveals that the drag force is $O(St^{-1})$, the virtual mass and the pressure gradient are $O((\rho/\rho_p)^1)$ and the Basset force is $O((\rho/\rho_p)^{1/2})$, where ρ and ρ_p are fluid density and particle density respectively. In our work, $\rho_p = 10^3 kg/m^3$ so that $\rho/\rho_p \simeq O(10^{-3})$. As shown by Chung and Troutt [28], the interaction between dispersed particles and vortical structures is also strongly dependent on the ratio of particle response time, τ_p, to the characteristic timescale of the structures encountered in the flow, τ_f. This ratio is commonly referred to as the Stokes number: The interaction mechanisms between flow and particles are such that a particle responds to flow structures having τ_f larger than or equal to their characteristic time, i.e. for $St \leq 1$, whereas particles tend to "cut across" the structures when $St > 1$ [4]. The Stokes number is defined as:

$$St = \frac{\tau_p}{\tau_f} \quad , \tag{4}$$

where $\tau_p = (\rho_p d_p^2)/(18\mu)$ is the particle response time, in which d_p is particle diameter. In this work, we chose the fluid timescale as defined in Eq. 2 and the corresponding values of the Stokes numbers are reported in Table 1.

Under the abovementioned assumptions, the Basset-Boussinesq-Oseen equation reduces to a balance of Stokes drag and inertia:

$$\frac{dv_i}{dt} = \alpha\{u_i\left[x_j(t), t\right] - v_i(t)\} \quad , \tag{5}$$

where $x_j(t)$ and $v_i(t)$ are the j-th and i-th components of particle position and velocity, respectively. Similarly, u_j is the j-th component of fluid velocity in the particle position. The parameter α is the inverse of particle response time, defined as:

$$\alpha = \frac{1}{\tau_p}\left(1 + 0.15 Re_p^{0.687}\right) \quad , \tag{6}$$

Table 1 Particle size and corresponding Stokes numbers

Particle diameter, d_p	Stokes number, St
10 μm	$6.67 \cdot 10^{-2}$
20 μm	$2.68 \cdot 10^{-1}$
50 μm	1.667

which includes the non-linear drag correction, and it is calculated considering the drag coefficient given by the formula [31]:

$$C_D = \frac{24}{Re_p}\left(1 + 0.15 Re_p^{0.687}\right) \quad , \tag{7}$$

where the particle Reynolds number is:

$$Re_p = \frac{|\,\vec{u} - \vec{v}\,|\, d_p}{\nu} \quad . \tag{8}$$

Given the abovementioned reasons, we believe that, for the specific flow systems examined here, the neglected terms either have a limited effect, or may induce a non realistic effect on particle motion.

As reported in previous works [33, 34], in LES-based Eulerian–Lagrangian simulations of particle dispersion a subgrid error is introduced in the particle equation since only the filtered fluid velocity is available. This approximation adds to the modeling error which is intrinsic to the SGS modeling for the fluid phase. Considering that there are still several open issues on how to model the influence of the filtered scales on particle motion [35, 37, 38], we felt that adding an SGS model for particles was not necessary for the current work, the focus of which is on the influence of the initial jet conditions.

We examined the two-way coupling issue with a similar approach. In this work, the dispersed fraction can be considered dilute in an average sense, and yet local accumulation can lead to regions where this approximation can break down. We are aware that initially particles have larger number concentration and that local accumulation can depend on the influence of the filtered small scales [35]. However, we decided to ignore the momentum coupling between the two phases for two main reasons. First, the two-way coupling would add just quantitative changes for the simulation parameters considered here (the two-way coupling allows to backscatter energy into the flow at a flow scale which is comparable to the particle scale; yet this flow scale does not match the frequency domain of the resolved part of the energy spectrum, which is actually affecting particle motion). Second, the model used to evaluate the two-way coupling effect would have introduced some uncertainty in the results which we can not cope with at the current stage of our research.

A Lagrangian particle tracking routine coupled with the DNS code was developed to calculate particle paths in the flow field. The routine uses a tri-linear interpolation method to obtain the fluid velocity at particle position. With this velocity the equations of particle motion are advanced in time using a fourth order RungeKutta scheme.

In the present Lagrangian tracking, three different particle diameters are considered, i.e. $d_p = 10$, 20 and 50 μm. These particles are initially randomly distributed within two specific regions of the inlet pipe: (i) the *inner* swarm is in the region extending from the pipe axis ($r = 0$) to 10 wall units from the pipe wall and (ii) the *outer* swarm is in the region extending from 10 wall units to the wall. Both particle clusters are initially located at the inflow within $z/r_m = 0$ and $z/r_m = 1$. This particle distribution generates the concentration profile sketched in Fig. 1a as $C(0)$, where δ is equal to 10 wall units. Each swarm (i.e. the *inner* and the *outer* one) counts 20 000 particles randomly dispersed and initial condition provides the velocity of each particle to be equal to that of the fluid in the same position. Such distribution

was used for two reasons. First the Lagrangian particle tracking is computationally expensive and we planned to have a large number of particles in the region where structures form. The second reason accounts for the behavior of particles in a straight, turbulent pipe flow: particles tend to have higher concentrations in the viscous sublayer [2, 3]. Particles released at the jet inlet are tracked over time until they reach the outlet section of the diffuser.

Particles moving along the diffuser may eventually reach the side wall. We simulated particle-wall collisions using the perfectly elastic assumption of specular reflection (perfect elastic rebound).

In this work, we did not consider particle-to-particle collisions. This assumption may have an effect in the initial region, where particle number concentration is higher. At the diffuser inlet, the volumic particle fraction for the outer 50 μm particles (the highest concentration) amounts to $4.71 \cdot 10^{-4}$. This value is high enough to produce a significant number of interparticle collisions, yet this is true only in the entrance region which is also influenced by the initial particle position which we set artificially. Downstream the boundary-layer separation, where our investigation is focused, particle swarm is rapidly spread over the high-vorticity region of the shear layer and is also immediately disgregated in the ring-shaped particle clusters produced by the action of the vortex rings. This causes a sudden decrease of the local particle volume fraction to values which make the occurrence of interparticle collisions extremely unlikely.

3 Results

3.1 Average flow

In this section, we will analyze particle behavior in connection with the flow structures. To this aim, it is important to describe first the dynamics of the flow.

The main characteristics of the flow simulated in this work are essentially those of a jet released from a circular nozzle, generating a potential core surrounded by a high–strain region which becomes progressively thicker as the jet proceeds downstream. This high–strain region is commonly called *shear layer* and separates the high velocity core region of the jet from a surrounding outer region. Time–averaged velocity profiles are expected to exhibit, immediately downstream of the separation point, intense radial gradients which progressively weaken while moving along the axis of the jet (coordinate z) as a consequence of the growth of the shear-layer thickness. The mean velocity profiles for a turbulent round free jet from Schlichting [40] can be used for a comparison with the present results as shown in Fig. 3a. The numerical profiles (symbols), computed by averaging in time and over the azimuthal coordinate θ, show a good agreement with the free jet in the inner jet region while the two flows behave differently in the external region. This difference is not surprising considering that, on account of the mass conservation, in a confined environment the spreading of the jet can only occur by generating a backflow with negative axial velocity in the external region. In a free jet, in contrast, the fluid can be entrained from outside into the jet without producing a parasite external flow. Since the external flow is increased by the jet entrainment, the agreement between free and confined jets decreases moving in the streamwise direction, as confirmed by

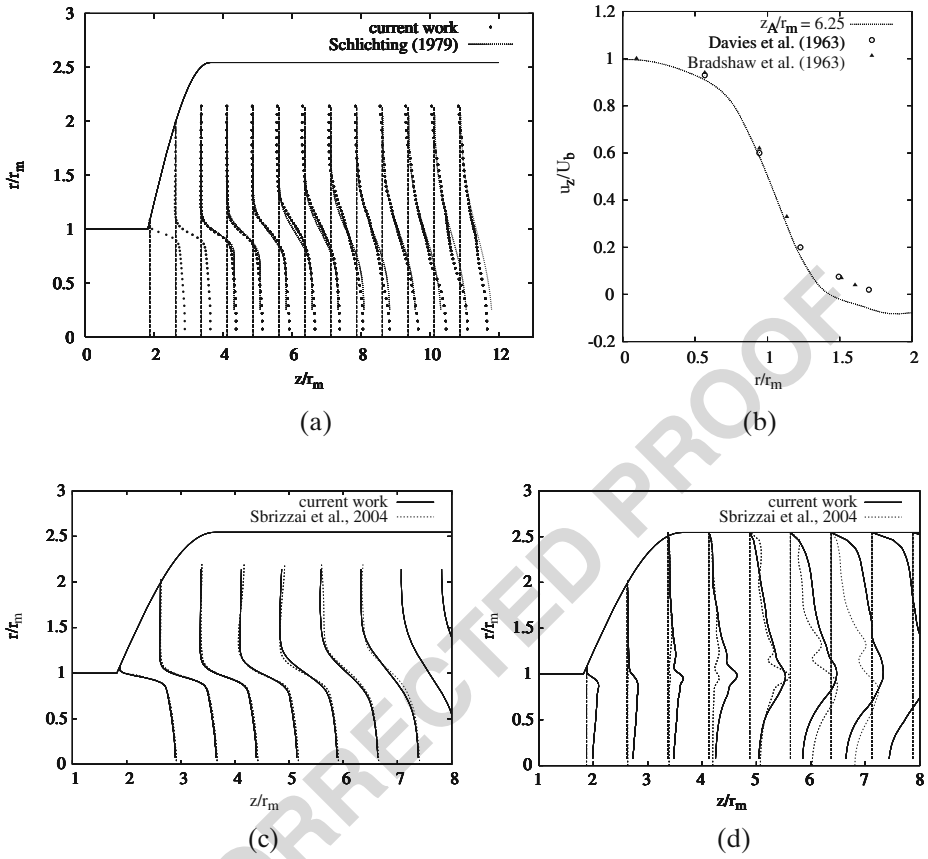

Fig. 3 Spatial evolution of the axial velocity profile (**a**) and comparison with experimental data on free jets at the beginning of the self-similar region (**b**). Comparison between time-averaged axial velocity profiles (**c**) and RMS of the axial velocity (**d**) obtained for the current work and for the case studied in Sbrizzai et al. [6]

Fig. 3a. A further comparison of the averaged flow field is given in Fig. 3b, where the axial velocity data of Davies et al. [41] and of Bradshaw et al. [42], obtained for free circular jets, are presented. These data refer, in both cases, to a specific distance from the nozzle, corresponding to $z/r_m \cong 6.25$ for the present configuration. As visible from Fig. 3b, a good agreement is found for the jet core corresponding to $r/r_m \cong 1.5$. Different velocity values are observed beyond $r/r_m > 1.5$, owing to the presence of the radial wall which causes the recirculation effect. These results are very similar to those obtained in our previous simulation.

To stress the differences between the present flow and that calculated in Sbrizzai et al. [6] we show a comparison between the time-averaged axial velocity profiles (Fig. 3c) and the RMS of the fluctuating part (RMS) of the axial velocity (Fig. 3d), obtained from the two different approaches.

In Fig. 3c we can notice that the time-averaged profiles are indeed very similar in the two cases. A slight difference can be observed downstream of $z/r_m \cong 5$, where

the jet fed by the turbulent pipe, calculated in the current simulation, exhibits a larger spreading, due to the dispersion produced by the upstream-advected turbulence.

The effectiveness of imposing a time-dependent fully-turbulent velocity profile upstream of the diffuser to reproduce the real conditions taking place in the diffuser is clearly evident from Fig. 3d. The RMS of the axial velocity shows that fluctuations already present in correspondence of the nozzle, only in the present case are successively spread over the whole width of the pipe, with higher values everywhere with respect to Sbrizzai et al. [6] in which significant fluctuations were observed only for $z/r_m > 3$. This denotes that structures generated locally in the shear layer are not sufficient to produce the spreading observed in such a geometry, a significant contribution being due to the upstream-generated turbulence.

3.2 Instantaneous flow features

Experimental observations on free circular jets [10] describe how instabilities of the initially straight shear layer lead to the formation of periodic annular vortices (or vortex rings) for moderately high values of the Reynolds number.

The intense velocity gradients observed in the shear layer trigger a Kelvin–Helmholtz instability which produces a periodic shedding of vortices, starting approximately one diameter downstream of the separation point ($z/r_m \cong 1.818$). A first qualitative overview of the flow structures can be obtained by the vorticity isocontours of Fig. 4, where a sequence of instantaneous flow fields, taken every $3\,\tau$, shows the formation and evolution of several vortical structures generated within the shear layer. Intense vorticity round nuclei are shed from the shear layer producing a pattern of ring vortices starting from $z/r_m \cong 4$, as visible from the snapshots of Fig. 4. It is interesting to note that, in the present case, characterized by the presence of upstream—generated turbulence at the inlet, the formation of the ring vortices is observed in the same position as in Sbrizzai et al. [6], where the inlet was fed by a prescribed laminar flow. The successive evolution of the flow however is quite different, being characterized in the present case by a larger radial spreading produced by the small scale dynamics.

Let us now focus on the downstream jet region, $z/r_m \geq 6$. in this region we can observe a sudden change in the flow, involving the formation of a variety of flow structures smaller than the Kelvin–Helmholtz (K–H) billows, which rapidly spread over the whole section of the downstream pipe (i.e. up to $r/r_m \cong 2.5$ – the external wall boundary), starting at $z/r_m \cong 8$. The phenomenon responsible for this sudden change of flow structure is the pairing of the ring vortices and the successive secondary instability which occurs around $z/r_m \cong 6$. Steps of this process are visible in the sequence of Fig. 4. In the panels (a), (b) and (c), we observe a couple of ring vortices separating from the shear layer and moving in the region $4 \leq z/r_m \leq 6$. Vortex rings get progressively closer, and a pairing eventually occurs in Fig. 4d. After the merging, the structures break up into smaller scales with irregular shape, that are immediately entrained in the jet core (Fig. 4e). Once these newly formed structures are advected downstream, they spread over the whole section of the large pipe and populate the region extending from $z/r_m \cong 6$ to the outlet.

We wish to stress that the above described dynamics is strongly three-dimensional and the flow in the meridional plane is coupled with the azimuthal direction mainly

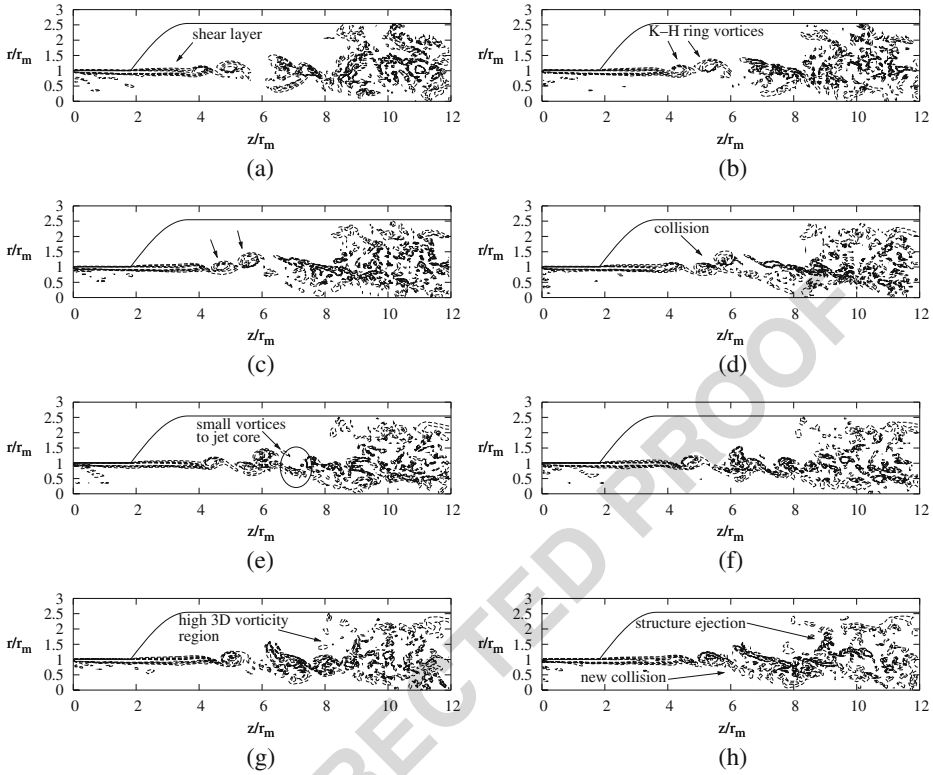

Fig. 4 Instantaneous vorticity isocontour sequence showing the pairing process occurring between subsequent Kelvin-Helmholtz vortex-rings. Snapshots are taken every 3 τ, starting from an arbitrary time instant (**a**–**h**)

through the ring instabilities; in the next section we will briefly describe the azimuthal flow dynamics.

3.3 Quantitative validation of vortex decay-rate by point-velocity statistics

A three-dimensional picture of the ring vortices may be useful to get an impression of their circumferential coherence, and especially of the progressive loss of geometric regularity while proceeding downstream. An efficient quantity to visualize position and dimensions of the vortices is the second invariant of the velocity gradient tensor:

$$Q = -\frac{1}{2}\left(\frac{\partial u_i}{\partial x_j}\frac{\partial u_j}{\partial x_i}\right) \quad . \tag{9}$$

Isosurfaces of Q help to identify the presence of different-size vortices in the flow field. A visualization of the ring vortices is given in Fig. 5, where three of these structures (I, II and III) are observed in the region between $z/r_m = 3.12$ and $z/r_m = 6.87$. In this figure, vortices are labeled progressively, starting from that located

JrnlID 10494_ArtID 9163_Proof# 1 - 09/06/08

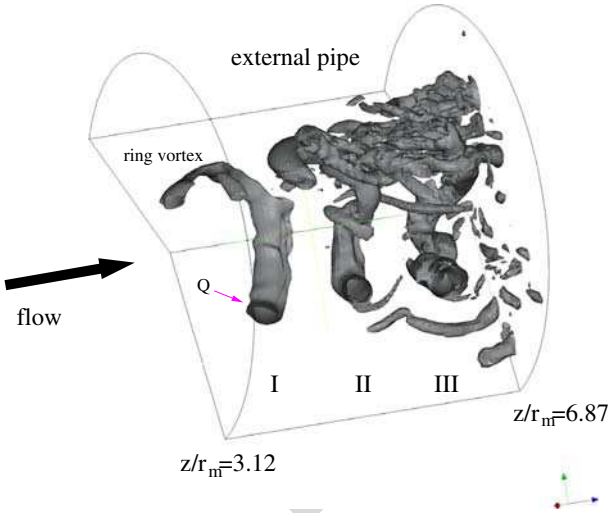

Fig. 5 Visualization of three subsequent vortex rings (I, II and III, respectively) by means of isocontours of Q (second invariant of the velocity gradient tensor) in the region $3.12 \leq z/r_m \leq 6.87$. Only a sector of about 200 *deg* in the azimuthal direction θ is shown for clarity

upstream (I is the closest to the nozzle), and moving in the positive z direction, where vortices II and III are encountered respectively.

It is evident that, differently from the ring vortices shown in our previous work [6], which were characterized by an extremely smooth shape, the presence of realistic inlet turbulence increases the ring instability and enhances the production of small scales. The structures of Fig. 5 show evident thickness variations along the azimuthal coordinate θ.

To describe from a quantitative viewpoint the progressive coherency loss of the ring vortices [10], we measured velocity signals in correspondence of diametrically–opposite points in the shear layer and we calculated the radial and axial velocity cross–correlations. Cross–correlation profiles are shown in Fig. 6, where a progressive decrease while proceeding along the axial direction. Results of Yule [10] for two air jets at Reynolds number equal to 9000 and 35 000 respectively, are also shown in Fig. 6. The values of cross correlation measured by Yule [10] show that vortex rings are formed as regular structures, characterized by an initially high circumferential coherence that progressively decays, this decay being faster as the Reynolds number increases. In our previous work [6] the absence of inflow turbulence generated a pattern of regular ring vortices, whose coherence remained close to unity for some diameters downstream. This produced a cross correlation curve completely different from those calculated by Yule [10], as visible in Fig. 6. In the present work, the increased complexity of the simulated flow allowed us to describe more faithfully the evolution of the flow structures, making it possible to compare the coherence decay of the ring vortices with the experiments. We evaluated the cross correlation through point measurements of the radial and axial velocity components at $r/r_m \cong 0.94$ at different z/r_m positions, corresponding to the range considered by Yule [10]; the results are given in Fig. 6 (dashed line without symbols). In this simulation, the Reynolds number is 17 516, which is intermediate between the values considered by Yule [10].

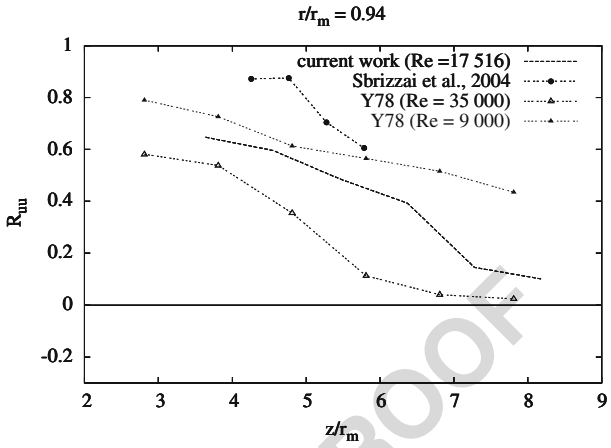

Fig. 6 Radial and axial velocity cross-correlation by point measurement at diametrally opposite locations of shear layer taken at different z positions

3.4 Interactions between particles and vortices: qualitative picture

Qualitative results on particle dispersion and entrainment are shown in Fig. 7, where the instantaneous particle position in an arbitrary meridional plane is reported together with instantaneous vorticity isocontours. Results are shown both for the outer particles, released within 10 wall units apart from the pipe wall, and for the inner particles, released in the central portion of the pipe. Figure 7 shows snapshots taken at $t = 10.909\ \tau$ for the inner 10 μm particles (a), 20 μm (b) and 50 μm (c) and at $t = 25.455\ \tau$ for the outer 10 μm particles (d), 20 μm (e) and 50 μm (f). Different representation time was chosen for the inner and the outer particles since the two swarms move with different velocities and reach the shear layer at different times.

In Fig. 7a, the 10 μm particles cluster in correspondence of different size vortices, i.e. both around the larger Kelvin–Helmholtz ring vortices, and the smaller structures generated after the pairing process, visible from $z/r_m \cong 8$ to $z/r_m \cong 10$, in Fig. 7a. A similar behavior is visible in Fig. 7d in the region from $z/r_m \cong 6$ to $z/r_m \cong 8$, showing that the 10 μm particles have a characteristic time smaller than that of most structures and for this reason such particles are easily entrained within the flow and have a large dispersion-rate.

The behavior of the 20 μm particles is illustrated in Figs. 7b and 7e. The transport of these particles is due to structures larger than those advecting the 10 μm particles. Accordingly, the smaller flow structures generated after the pairing of the primary Kelvin–Helmholtz billows are basically ignored by the dynamics of the 20 μm particles, as is evident in Fig. 7b where a larger cluster is observed around $z/r_m \cong 10$. This cluster is characterized by a higher particle concentration (denoted by a larger thickness with respect to that observed for the 10 μm) and well defined borders. Well–defined clusters are also visible in Fig. 7e for the outer 20 μm particles, both in correspondence of subsequent ring vortices observed within $z/r_m \cong 4$ and $z/r_m \cong 6$ and further downstream, around $z/r_m \cong 8$.

Figure 7c and f show that the 50 μm particles respond only to the coherent vortex rings and tend to cut across the whole variety of structure formed after the pairing process, as denoted by the large swarm observed in Fig. 7c from $z/r_m \cong 9$ to $z/r_m \cong 11$, which moves downstream mostly under the action of the jet core. In Fig. 7f, outer

JrnlID 10494_ArtID 9163_Proof# 1 - 09/06/08

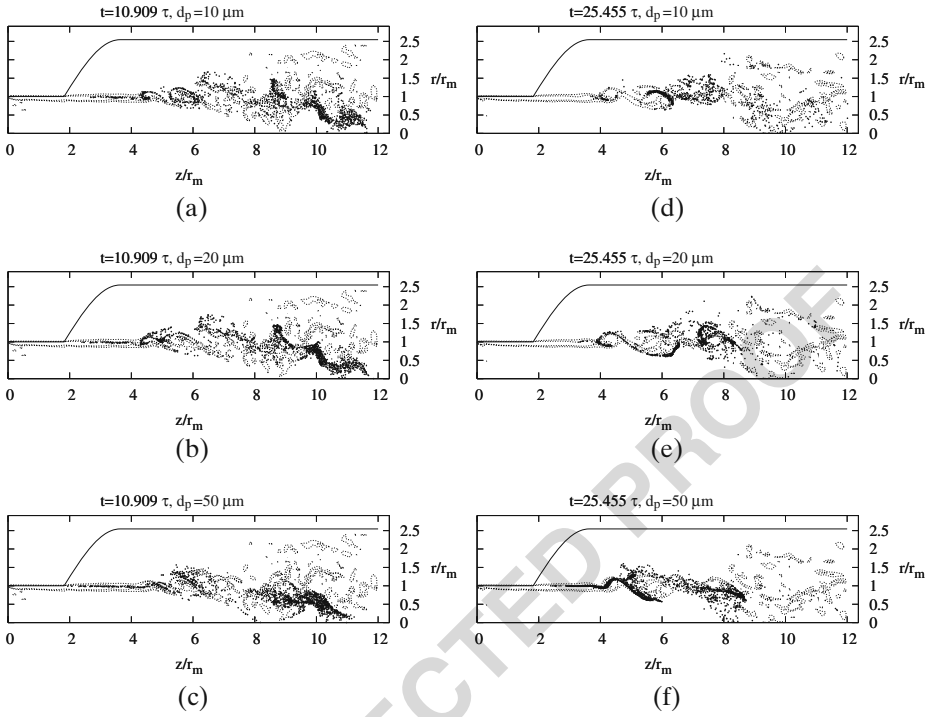

Fig. 7 Snapshots of instantaneous particle position and instantaneous vorticity isocontours taken at different time for the inner and outer particles. Inner 10 μm (**a**), 20 μm (**b**) and 50 μm particles (**c**) are shown at time $t = 10.909\ \tau$ from release; outer 10 μm (**d**), 20 μm (**e**) and 50 μm particles (**f**) are shown at $t = 25.455\ \tau$, respectively

50 μm particles show to collect preferentially around the very large billow present at about $z/r_m \cong 6$ and to ignore the structure at $z/r_m \cong 8$ which instead is able to entrain the 20 μm particles.

3.5 Particle dispersion

To examine the lateral dispersion, we computed the root mean square displacement (RMSD) of particles in the radial direction measured around the center of mass of the swarm. The time evolution of the position of the center of mass of the swarm is calculated as:

$$x_G(t) = \frac{1}{N}\sum_{j=1}^{N}\left[x_j(t)\right] \quad ; \quad y_G(t) = \frac{1}{N}\sum_{j=1}^{N}\left[y_j(t)\right] \quad ; \quad z_G(t) = \frac{1}{N}\sum_{j=1}^{N}\left[z_j(t)\right] \quad . \tag{10}$$

The RMSD is then calculated as:

$$RMSD(t) = \sqrt{\frac{1}{N}\sum_{j=1}^{N}\left[x_j(t) - x_G(t)\right]^2 + \left[y_j(t) - y_G(t)\right]^2} \quad ; \tag{11}$$

where N is the total number of particles, $x_j = r_j \cos\theta_j$ and $y_j = r_j \sin\theta_j$, r_j and θ_j being the radial and azimuthal coordinates of the j-th particle at a given time.

In the investigated flow we expect that particles move together with the jet core along the axial direction, z, and thus to observe large-scale motions along the same direction. Since we are mostly interested in the sideways dispersion, useful to quantify the spreading of a continuous flow of particles moving along a jet, we decided to evaluate the RMSD along the radial direction only, where flow motions are predominantly due to structures generated by the instabilities of the shear layer and not directly from the main flow direction. We are not showing the dispersion rates along the axial direction since the phenomenon of "shear dispersion" will dominate the quantitative figures. The calculation of the particle dispersion along the axial direction is also less significant in the case of a continuous particle release.

The time-history of the centre of mass in the z direction, computed as from equation (10) is shown in Fig. 8a and b for the inner and outer particles, respectively. The RMSD is shown in Fig. 8c for the inner particle swarm and in Fig. 8d for the outer particle swarm as a function of z_G. By observing Fig. 8a–b one can notice that the final position of the centre of mass of the swarms lies downstream as the particle diameter (i.e. mass) increases for the inner particles, whereas the opposite

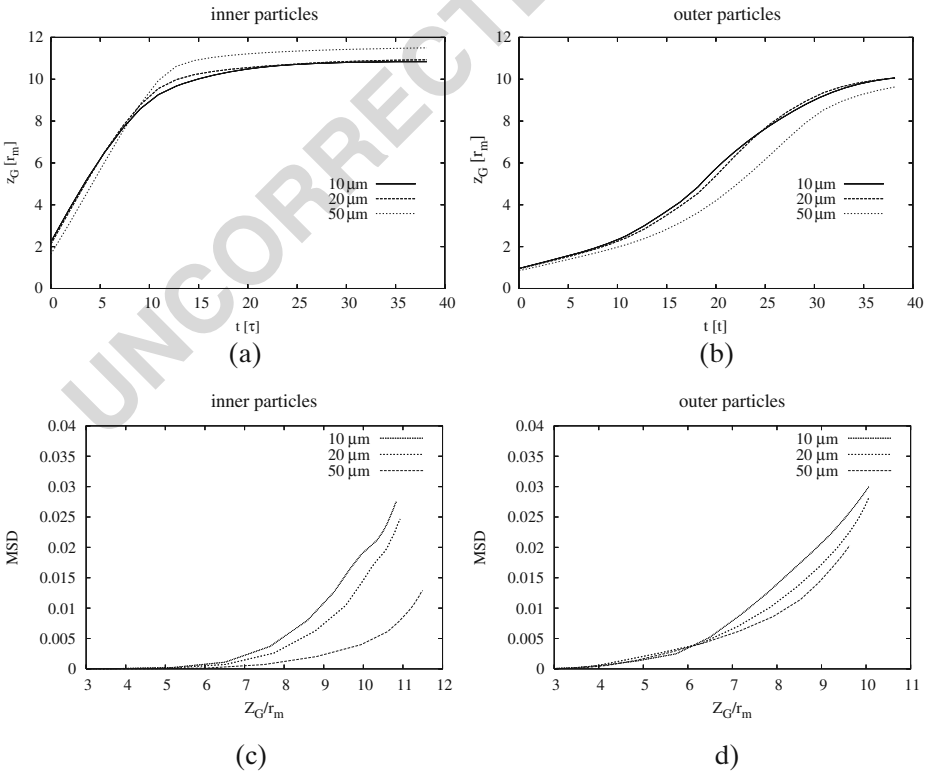

Fig. 8 Time-history of the mass centre for the inner (**a**) and outer (**b**) particle swarms and mean square displacement of the inner (**c**) and outer (**d**) particles swarms. Dispersion is shown as a function of the axial position of the center mass of particle swarms, Z_G

occurs for the outer particles. This can be explained by considering that inner 10 μm particles are transported outside the shear layer (that is, in the outer region) where flow velocities are almost zero, whereas larger particles tend to remain in the jet core and are convected downstream in larger amounts. The behavior of the outer swarm, which has been released close to the inlet pipe wall where the flow velocity is rather low, is instead due to the lower initial particle momentum. The fluid velocity rapidly increases after separation (in the shear layer), while particles lag the fluid with a delay proportional to the square of their diameter as from the definition of their time scale.

Results reporting the RMSD behavior are shown in Fig. 8c, d and indicate that smaller 10 μm particles spread faster than the others, reaching high dispersion values both for the inner and for the outer swarms. Larger 20 μm particles exhibit slightly smaller dispersion whereas remarkable difference is observed for the inner 50 μm particles, the behavior of which is represented by the thicker dashed line. These particles show to disperse less than the others. Outer 50 μm particles of Fig. 8d, in contrast, closely follow the trend of the 10 and 20 μm particles and have dispersion rate higher with respect to the same particles in the inner swarm. This difference is due to the different position occupied by the swarms during the interaction with the flow, respectively in the jet core and in the shear layer. In the shear layer region, the large and more energetic structures are able to entrain and disperse the particles in radial and azimuthal directions more efficiently than the smaller vortices of the jet core which, although interacting with all particles, lack the required energy.

3.6 Particle-velocity autocorrelation and Lagrangian timescale

Together with the evolution of particle dispersion around the initial position, the velocity of the particles is also characterized by a progressive loss of correlation with the initial values.

This loss of velocity correlation can be quantified by calculating the particle velocity autocorrelation [43]:

$$R_{L,i}(\tau) = \frac{\frac{1}{N}\sum_{j=1}^{N}\left[v_i(t_0)\cdot v_i(t_0+\tau)\right]}{\frac{1}{N}\sum_{j=1}^{N} v_i^2(t_0)}, \tag{12}$$

where v_i is the velocity of the particle in the x_i direction, and t_0 is a reference time. The time interval over which the particle velocity is correlated with itself can be evaluated through the Lagrangian timescale:

$$T_{L,i} = \int_0^{+\infty} R_{L,i}dt. \tag{13}$$

In the present work, the particle velocity autocorrelation is calculated with respect to a reference time t_0 at which most particles are found within "active" regions of the flow, i.e. in the shear layer, where the interactions with the flow are stronger. The value of t_0 was chosen equal to 21.82τ and 27.28τ for the inner and outer particles, respectively. Results are shown in Fig. 9 for the azimuthal (panels a) and b) and radial components (panels c) and d) of the autocorrelation function respectively. With reference to Fig. 9e–f, We observe that the Lagrangian timescale of the larger 50 μm particles is always larger than that for the smaller particles for all the three

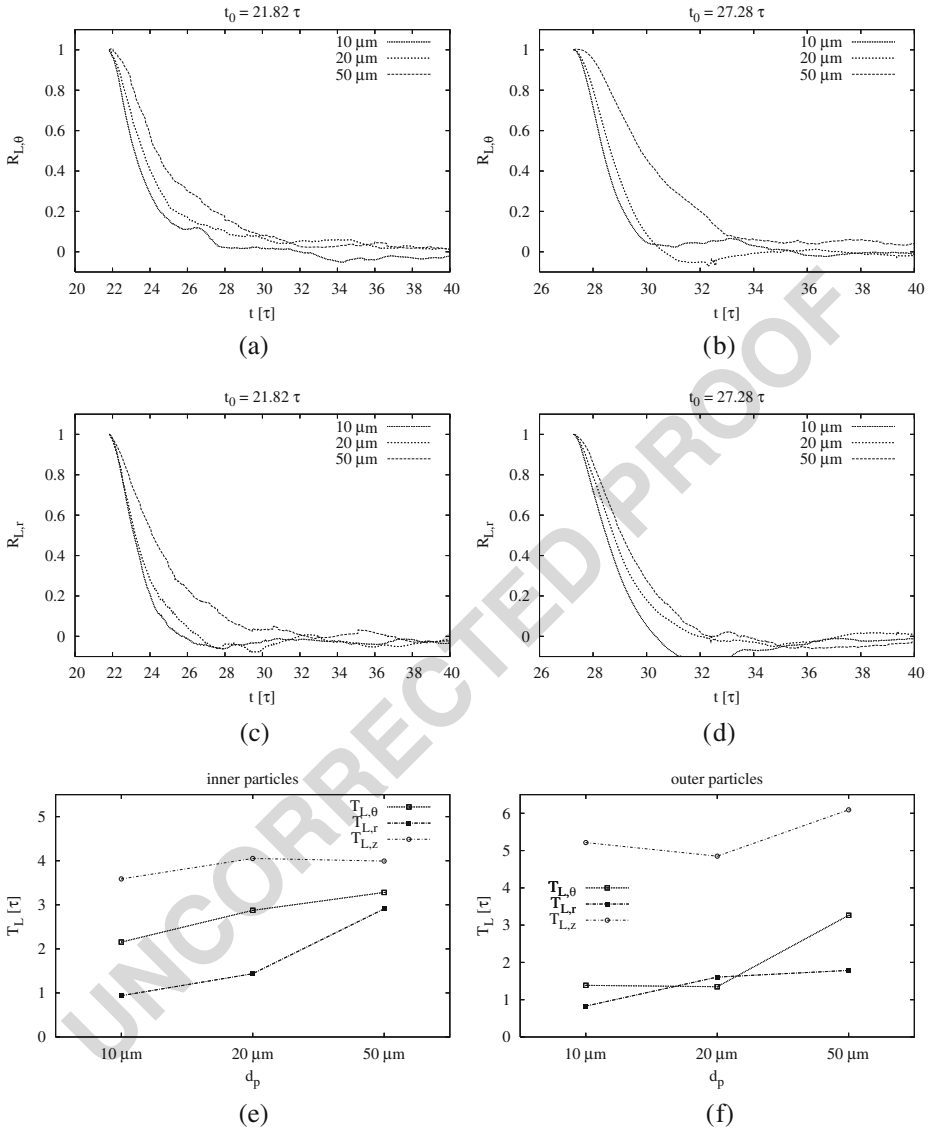

Fig. 9 Particle-velocity autocorrelation for the azimuthal and radial velocity components and Lagrangian integral timescale at the end of simulation. Figures **a**) and **b** show velocity autocorrelation, $R_{L,\theta}$, of the azimuthal component, u_θ, for the inner and outer particles, respectively. Figures **c** and **d** show velocity autocorrelation, $R_{L,r}$, of the radial component, u_r for the inner and outer particles, respectively. Figures **e** and **f** show the Lagrangian timescale, τ_L, of inner and outer particles evaluated at the end of simulation

components of the velocity. This result frames the notion that larger particles have larger inertia in the context of our flow field, indicating that at the end of the simulation time such large particles still have memory of their past.

4 Conclusions

In this work we examined the problem of the turbulent flow in a long circular pipe issued in a large angle abrupt diffuser. We also considered the presence of a dispersed phase constituted by a large number of small particles with the density of the water and characterized by three different diameters. This configuration is encountered in a number of technological applications in which the crucial variable is the degree of interphase mixing achieved downstream the diffuser. The behavior of the particle-flow system is complex and characterized by a number of different spatial and temporal scales mutually interacting and contributing to the particle dispersion. With the current work we wanted to overcome the limits of our previous simulation [6]. In particular, we considered explicitly the influence of inlet turbulence on the downstream evolution of the flow structures and in turn on particle dispersion. To this purpose, we used a Large Eddy Simulation of a turbulent pipe at $Re = 17\,516$ to supply a time-dependent fully turbulent inlet profile to a pipe expansion also simulated by means of Large Eddy Simulation.

The examination of the flow field shows a good agreement with analogous flow configurations such as free circular jets, both in time averaged velocity profiles and in the decay rate of coherent structures formed within the shear–layer and gives quantitative figures for the influence of the inlet turbulence on the downstream flow structure and velocity statistics.

Three distinct regions of the flow are formed after separation of the pipe boundary layer: a jet core, a shear–layer and an outer region. The intense velocity gradients present in the shear layer are responsible for the formation of an array of ring vortices periodically shed from about one diameter downstream of the separation point.

Comparison against our previous simplified simulation [6] has shown that the position at which the ring vortices are formed is not influenced by the presence of upstream-generated turbulence. However, the turbulence scales issued by the cylindrical pipe have a strong effect on spreading and on entrainment of the jet. This is due to the amplification of the inlet perturbations through the azimuthal instability of the vortex rings that, in the present study, are more distorted.

Contiguous vortex rings are observed to pair at about $z/r_m \cong 6$ in a merging process which produces a variety of smaller structures. This merging marks the transition between an upstream *transitional* flow and a downstream *turbulent* flow, that is identified by the presence of a three-dimensional vorticity field and by large, non-coherent structures called *eddies* by Yule [10]. Smaller structures are entrained in the jet core, advected downstream and eventually expelled towards the outer region from about $z/r_m \cong 8$, where the turbulent flow extends up to the external wall of the diffuser pipe.

A detailed examination of the behavior of the dispersion of 10 μm, 20 μm and 50 μm particles show that particles interact with vortices in different manners, depending on the particle-to-structure timescale ratio (Stokes number). Smaller 10 μm particles are rapidly entrained by the large structures in the near–field of the jet and then spread over the whole section of the pipe after the pairing process, showing the highest dispersion at the end of simulation, as well as the highest dispersion rate. Intermediate size 20 μm particles show a tendency to form clusters around structures with timescale matching the particle characteristic time. These particles disperse less than the 10 μm particles. Larger 50 μm particles tend to cut

across most of the flow structures and their motion appears to be influenced by the largest vortices.

Results on particle dispersion obtained computing the Mean Square Displacement show that the 10 μm and the 20 μm particles exhibit larger dispersion with respect to the 50 μm particles. This seems due to the strong interactions with flow structures observed after the pairing process. These structures are too small to entrain the 50 μm particles, which tend to follow the larger Kelvin–Helmholtz ring vortices and the main flow. Appreciable dispersion of the 50 μm particles is observed for the outer swarm since this is released in the shear layer, where the larger vortices form.

Particle velocity autocorrelation and Lagrangian timescale are used to evaluate quantitatively the dispersion time expected for a given particle diameter. Results confirm the previous observations that the 10 μm and the 20 μm particles, responding to the smaller and faster structures, are quickly dispersed within the flow, whereas the 50 μm particles follow the large Kelvin–Helmholtz vortices, and undergo a relatively longer dispersion process.

References

1. Moin, P., Apte, S.V.: Large-eddy simulation of realistic gas turbine combustors. AIAA J. **44**, 698–708 (2006)
2. Marchioli, C., Soldati, A.: Mechanisms for particle transfer and segregation in turbulent boundary layer. J. Fluid Mech. **468**, 283–315 (2002)
3. Marchioli, C., Giusti, A., Salvetti, M.V., Soldati, A.: Direct numerical simulation of particle wall transfer and deposition in upward turbulent pipe flow. Int. J. Multiph. Flow **29**, 1017–1038 (2003)
4. Soldati, A.: Particles turbulence interactions in boundary layers. ZAMM J. Appl. Math. Mech. **85**, 683–699 (2005)
5. Righetti, M., Romano, G.P.: Particle-fluid interactions in a plane near-wall turbulent flow. J. Fluid Mech. **505**, 93–121 (2004)
6. Sbrizzai, F., Verzicco, R., Pidria, M.F., Soldati, A.: Mechanisms for selective radial dispersion of microparticles in the transitional region of a confined turbulent round jet. Int. J. Multiph. Flow **30**, 1389–1417 (2004)
7. Salvetti, M.V., Orlandi, P., Verzicco, R.: Numerical simulations of transitional axisymmetric coaxial jets. AIAA J. **34**, 736–743 (1996)
8. Akselvoll, K., Moin, P.: Large-eddy simulation of turbulent confined coannular jets. J. Fluid Mech. **315**, 387–411 (1996)
9. Na, Y., Moin, P.: Direct numerical simulation of a separated turbulent boundary layer. J. Fluid Mech. **370**, 175–202 (1998)
10. Yule, A.J.: Large-scale structures in the mixing layer of a round jet. J. Fluid Mech. **89**, 413–432 (1978)
11. Hussain, A.K.M.F., Clark, A.R.: On the coherent structure of the axisymmetric mixing layer: a flow-visualization study. J. Fluid Mech. **104**, 263–294 (1981)
12. Hussain, A.K.M.F.: Coherent structures and incoherent turbulence. In: Tatsumi, T. (ed.) Turbulence and Chaotic Phenomena in Fluids, p. 453. North-Holland, Amsterdam (1983)
13. Hussain, A.K.M.F.: Coherent structures and turbulence. J. Fluid Mech. **173**, 303–356 (1986)
14. Verzicco, R., Orlandi, P.: A finite-difference scheme for the three dimensional incompressible flows in cylindrical coordinates. J. Comput. Phys. **123**, 402–414 (1996)
15. Longmire, E.K., Eaton, J.K.: Structure of a particle laden-round jet. J. Fluid Mech. **236**, 217–257 (1992)
16. Ovchinnikov, V., Piomelli, U., Choudhari, M.M.: Numerical simulations of boundary-layer transition induced by a cylinder wake. J. Fluid Mech. **547**, 413–441 (2006)
17. Orlandi, P., Fatica, M.: Direct simulations of turbulent flow in a pipe rotating about its axis. J. Fluid Mech. **343**, 43–72 (1997)

18. Schmidt, S., Mclver, M.D., Blackburn, H.M., Rudman, M., Nathan, G.J.: Spectral element based simulations of turbulent pipe flow. In: 14th Australasian Fluid Mech. Conf., Adelaide, 9–14 December 2001
19. Verzicco, R., Orlandi, P. Eisenga, A.H.M., Van Heijst, G.J.: Dynamics of a vortex ring in a rotating fluid. J. Fluid Mech. **317**, 215–239 (1996)
20. Orlandi, P.: Fluid Flow Phenomena. A Numerical Toolkit. Kluwer Academic, London (2000)
21. Kim, J., Moin, P.: Application of a fractional-step method to incompressible Navier-Stokes equations. J. Comput. Phys. **59**, 308–323 (1985)
22. Le, H., Moin, P.: An improvement of fractional-step methods for the incompressible Navier-Stokes equations. J. Comput. Phys. **92**, 369–379 (1991)
23. Germano, M., Piomelli, U., Moin, P., Cabot, W.H.: A dynamic subgrid-scale eddy viscosity model. Phys. Fluids **3**(7), 1760–1765 (1991)
24. Fadlun, E.A., Verzicco, R., Orlandi, P., Mohd-Yusof, J.: Combined immersed-boundary/finite-difference methods for three-dimensional complex flow simulations. J. Comput. Phys. **161**, 35–60 (1986)
25. Lowery, P.S., Reynolds, W.C.: Numerical simulation of a spatially-developing, forced, plane mixing layer. Rep. TF-26, Thermosciences Division, Dept. of Mech. Engng, Stanford University (1986)
26. Pauley, L.L., Moin, P., Reynolds, W.C.: A numerical study of unsteady laminar boundary layer separation. Rep. TF-34, Thermosciences Division, Dept. of Mech. Engng, Stanford University (1988)
27. Crowe, C., Sommerfeld, M., Tsuji, Y.: Multiphase flow with droplets and particles. CRC, Boca Raton (1998) Q4
28. Chung, J.N., Troutt, T.R.: Simulation of particle dispersion in an axisymmetric jet. J. Fluid Mech. **186**, 199–222 (1988)
29. Loth, E.: Numerical approaches for motion of dispersed particles, droplets and bubbles. Prog. Eng. Comb. Sci. **26**, 161–223 (2000)
30. Maxey, M.R., Riley, J.J.: Equation of motion for a small rigid sphere in a nonuniform flow. Phys. Fluids **26**(4), 883–889 (1983)
31. Rowe, P.N., Enwood, G.A.: Drag forces in hydraulic model of a fluidized bed – Part I. Trans. Inst. Chem. Eng. **39**, 43–47 (1962)
32. Kim, I., Elghobashi, S., Sirignano, W.A.: On the equation for spherical-particle motion: effect of Reynolds and acceleration numbers. J. Fluid Mech. **367**, 221–253 (1998) Q5
33. Kuerten, J.G.M., Vreman, A.W.: Can turbophoresis be predicted by large-eddy simulation?. Phys. Fluids **17**, Art. No. 011701 (2005)
34. Kuerten, J.G.M.: Subgrid modeling in particle-laden channel flow. Phys. Fluids **18**, Art. No. 025108 (2006)
35. Fede, P., Simonin, O.: Numerical study of the subgrid fluid turbulence effects on the statistics of heavy colliding particles. Phys Fluids **18**, Art. No. 045103 (2006)
36. Armenio, V., Piomelli, U., Fiorotto, V.: Effect of the subgrid scales on particle motion. Phys. Fluids **11**, 3030–3042 (1999) Q5
37. Shotorban, B., Mashayek, F.: Modeling subgrid-scale effects on particles by approximate deconvolution. Phys. Fluids **17**(8), Art. No. 081701 (2005)
38. Marchioli, C., Salvetti, M.V., Soldati, A.: Some issues concerning Large–Eddy–Simulation of inertial particle dispersion in turbulent flows. Phys. Fluids **20**, Art. No. 045100 (2008)
39. Picciotto, M., Marchioli, C., Soldati, A.: Characterization of near-wall accumulation regions for inertial particles in turbulent boundary layers. Phys. Fluids **17**, 098101 (2005) Q5
40. Schlichting, H.: Boundary-Layer Theory, 7th edn. McGraw-Hill, New York (1979)
41. Davies, P.O.A.L., Fisher, M.J., Barratt, M.J.: The characteristic of the turbulence in the mixing region of a round jet. J. Fluid Mech. **15**, 337–367 (1963)
42. Bradshaw, P., Ferriss, D.H., Johnson, R.F.: Turbulence in the noise-producing region of a circular jet. J. Fluid Mech. **19**, 591–624 (1964)
43. Hinze, J.O.: Turbulence, pp. 211–215. McGraw-Hill, New York (1975)
44. Fessler, J.R., Kulick, J.D., Eaton, J.K.: Preferential concentration of heavy particles in a turbulent channel flow. Phys. Fluids **6**(11), 3742–3749 (1994) Q5